Screening of hydrogen bonds in modified cellulose acetates with alkyl chain substitutions

(article starts on next page)

Screening of hydrogen bonds in modified cellulose acetates with alkyl chain substitutions

Robin Nilsson [a,b], Martina Olsson [c], Gunnar Westman [b,d], Aleksandar Matic [b,c], Anette Larsson [a,b,*]

[a] *Applied Chemistry, Department of Chemistry and Chemical Engineering, Chalmers University of Technology, SE-412 96 Gothenburg, Sweden*
[b] *FibRe-Centre for Lignocellulose-based Thermoplastics, Department of Chemistry and Chemical Engineering, Chalmers University of Technology, SE-412 96 Gothenburg, Sweden*
[c] *Materials Physics, Department of Physics, Chalmers University of Technology, SE-412 96 Gothenburg, Sweden*
[d] *Chemistry and Biochemistry, Department of Chemistry and Chemical Engineering, Chalmers University of Technology, SE-41296 Gothenburg, Sweden*

A B S T R A C T

This study aimed to elucidate how the glass transition temperature and water interactions in cellulose esters are affected by the structures of their side chains. Cellulose acetate, cellulose acetate propionate and cellulose acetate butyrate with three fractions of butyrates, all having the same total degree of substitution, were selected, and hot-melt pressed. The degree of substitution, structural properties, and water interactions were determined. The Hansen solubility parameters were calculated and showed that the dispersive energy dominates the total cohesive energy, followed by hydrogen bonding and polar energy. The glass transition temperature (T_g) decreased, counter-intuitively, with an increased total cohesive energy, which can be explained by the short-range hydrogen bonds being screened by the increased length of the substituents. The solubility and penetration of water in the cellulose esters decreased with increased side chain length, although the hydrogen bonding energies for all the esters were approximately constant.

1. Introduction

Modifying cellulose adds value to the most abundant biopolymer found on the planet, where the starting material for substitution can be derived from plants, wood or other sources such as recycled newspapers (Filho et al., 2008), waste blended fabrics (Sun et al., 2013) or sorghum straw (Andrade Alves et al., 2019). The type and degree of substitution (DS) per anhydroglucose units (AGUs) create enormous opportunities to tune the hydrophobicity, mechanical and thermal properties of the cellulose derivatives. The influence of the substituent can be demonstrated by comparing methylcellulose and ethyl cellulose, where a similar degree of substitution allows the former to dissolve in water but the latter not (Hjärtstam & Hjertberg, 1999a; Kono & Numata, 2020). A large variety of cellulose derivatives are currently available commercially: a few substituted cellulose ethers that may be mentioned in this context are methyl cellulose, ethyl cellulose (EC), hydroxyethyl cellulose, hydroxypropyl cellulose (HPC), hydroxypropyl methylcellulose (HPMC), ethyl hydroxyethyl cellulose, methyl ethyl hydroxyethyl cellulose, and a few substituted cellulose esters are cellulose acetate (CA), cellulose acetate propionate (CAP), cellulose acetate butyrate (CAB) and cellulose acetate phthalate. Cellulose derivatives are commercially attractive because they are made from renewable sources and easily tuned to provide desirable properties. This ability makes them useful in a large variety of applications, such as coatings, laminates, additives in building materials, pharmaceuticals, cosmetics, optical films and food (Klemm et al., 2005). In many of these products, cellulose derivatives are the component that provides the product with its critical function: one example is the cellulose ether HPMC, which is used as a release-controlling agent for drug delivery from hydrophilic matrix tablets (Viriden et al., 2010). Other examples are HPC and EC: their phase separation in coatings is used to control the drug delivery (Andersson, 2015). Cellulose esters, like cellulose acetate, are known to have good barrier properties in food packaging and are also used in coatings, lacquers, sealants and pharmaceutical applications (Gabor & Tita, 2012;

Schuetzenberger et al., 2016). Moreover, cellulose ester films exhibit good mechanical properties and are used as membranes in separation techniques (Klemm et al., 2005). CA in particular, along with CAP and CAB, has attracted interest in the field of water purification by reversed osmosis, as well as the newer technology of forward osmosis, due to their ability to tune water fluxes and salt retention (Ong et al., 2012; Ong & Chung, 2012; Qiao et al., 2012; Zhang et al., 2012). Fully substituted CA, commonly referred to as cellulose triacetate, has high salt retention but low water flux, whereas less substituted CA has higher water flux and lower salt retention. CAP and CAB have a lower salt and water permeability than CA: properties that are shown to depend on the substitution degree (Ong et al., 2012).

The transport of permeants in polymer films, which is determined by several factors such as the solubility of the permeant and the diffusion coefficient for the permeant in the film, has been discussed in the review paper by Gårdebjer et al. (Gårdebjer et al., 2018). Crystallinity affects the diffusion rate in at least two ways: firstly, the crystalline regions are almost impermeant, resulting in longer diffusion pathways and consequently a decrease in total solubility. Secondly, the tie chains between the crystalline regions decrease the chain mobility, resulting in a lower diffusion rate (Ashley, 1985). These effects on permeability have been confirmed by increased crystallinity found at interphases between laminar structures (polyethylene and modified polyethylene) by Gårdebjer et al. and poly(lactic acid) with nanofillers by Trifol et al. (Gårdebjer, Andersson, et al., 2016; Gårdebjer, Gebäck, et al., 2016; Trifol et al., 2020). The mobility of the chain is also affected by the temperature relative to the glass transition temperature (T_g) and thus relates directly to the barrier properties (Ashley, 1985). The T_g is known to depend on several factors, including the intermolecular forces between the polymer chains, the space occupied by the main chain and side chains, the movement of the side chains and density (Kreibch & Batzer, 1979).

Water is recognized as absorbing into many biopolymers and having a plasticizing effect (Reid & Levine, 1991). The amount of water absorbed depends on the environment, e.g. the relative humidity and temperature, and thereby affects the properties of the material. The tailoring of new bio-based materials can be improved by increasing knowledge of how water interacts with the polymers, so that its effect on the properties of the material can be predicted more skilfully. The amount of -OH groups present in bio-based polymers has been used to make such predictions in the literature, since these groups have been proven to be of importance to both interactions with water (Akim, 2005; Ong et al., 2013) and thermal properties such as the T_g (Asai et al., 2001; Hjärtstam & Hjertberg, 1999b). A common concept used to predict interactions between polymers and solvents was launched by Hansen and is often referred to as Hansen solubility parameters (HSP). These have been applied to several areas, including polymer solubility, swelling in solvents, surfaces-solvent interaction and, in particular, barrier properties (Hansen, 2007). HSP are based on three different types of interactions: dispersion cohesive energy (E_D), polar cohesive energy (E_p) and hydrogen bonding energy (E_H). The parameters can either be determined experimentally via the degree of swelling or solubility in several well-defined solvents, or calculated bottom-up using group contribution methods. Interactions between solvents and polymers calculated by the HSP concept have been shown to correlate to solubility and permeability, making it a suitable tool for analysing polymers and permeant interactions (Lindblad et al., 2008).

This study aims at evaluating how the molecular structures of the various substituents in the cellulose acetate derivatives CA, CAP, and CAB affect interactions with water and the T_g. The hypothesis in this study is that an increasing side chain length decreases the effect of the hydrogen bonding and thus screens attractive interactions that affect thermal properties and the polymers' interaction with water. Therefore, cellulose derivatives with a similar total number of substituents were chosen but with different side chain lengths and ratios between shorter and longer side chains. The film-forming process employed here is solvent-free hot-melt pressed films, which is in contrast to the majority of permeation studies that use solvent-cast films (Lee et al., 2018; Lonsdale et al., 1965). When solvent interacts strongly with the polymer chains, there is a risk that small amounts of solvents remain in the film after film casting and may thereby influence its properties. The cellulose derivatives were hot-melt pressed into films and characterized by FTIR, NMR, TGA, DSC and WAXS before studying the water absorption and water permeation. The NMR data was used to calculate the degree of substitution; based on these, the HSP were calculated and correlated to T_g, water absorption and water permeation.

2. Experimental

2.1. Materials

Cellulose acetate (CA, number average molecular weight, $M_n = 50$ kDa), cellulose acetate propionate (CAP, $M_n = 75$ kDa), cellulose acetate butyrate of three different degree of substitutions and referred to as CABI ($M_n = 65$ kDa), CABII ($M_n = 30$ kDa) and CABIII ($M_n = 30$ kDa), were all purchased from Sigma Aldrich, Sweden. Ethyl cellulose (EC) (CR grade 14 cPs) was kindly provided by DowWolff Cellulosics GmbH, Germany. All polymers were used as received. Intervals of the number of substituents on each cellulose derivative were provided by the suppliers, and these are presented in Table S1, in Supporting information (SI).

Potassium bromide FT-IR grade, ≥99% from Merck, DMSO-D_6 sourced from VWR, and Chloroform-*d* 99.8 atom % D were purchased from Sigma Aldrich Sweden. In the diffusion measurements, 5 mCi (185 MBq) tritium-labeled water and Ultima Gold from Perkin–Elmer, USA, were used.

2.2. Sample preparation

Hot-melt pressing was used to prepare thin films of 100 μm for the water self-diffusion experiments and 500 μm thick films for the water absorption experiments. The materials, approx. 0.2 g for thin films and 0.5 g for thick films, were pressed between two flat metal plates for 5–7 min under 15 ± 0.5 t pressure at a temperature of 10–30 °C above the melting temperature of each material but below their degradation temperature. The films were pressed at: 260, 210, 250, 190, 170 and 180 °C for CA, CAP, CABI, CABII, CABIII and EC, respectively. Thereafter, the flat plates with sample film conditioned for more than 30 min at room temperature at a pressure of 8.9 ± 0.1 kg until the temperature was below 60 °C, before samples were shaped into suitable dimensions for the respective analysis method.

2.3. FTIR

The cellulose derivatives were mixed to 1 wt% with KBr, ground into powder using a mortar and pestle and then pressed into tablets. The Fourier transform infrared (FTIR) spectra were obtained on a PerkinElmer Spectrum One FTIR Spectrometer (PerkinElmer instruments, Massachusetts, USA), with 28 scans per sample, a resolution of 4 cm^{-1} at 400–4000 cm^{-1}, for samples stored in a desiccator and measured directly.

2.4. NMR

CA was dissolved in DMSO-D6 (40 mg mL^{-1}) and characterized with ^{1}H NMR on an Agilent 400 MHz spectrometer with eight scans and acquisition time of 2.5559 s. ^{1}H-^{1}H gCOSY (gradient correlation spectroscopy) experiment was performed with the standard gCOSY Varian sequence using one scan and 128 increments. Spectral widths of 8 ppm in both directions with a 3.3 kHz spectral width, 0.15 s acquisition time, 1 s relaxation delay and 9.6 μs 90° pulse width were used. The other cellulose derivatives were dissolved in CDCl$_3$ and analysed in the same way. The degree of substitutions (DS) for the acetates were calculated

according to Huang et al. (2011), using Eqs. (1), (2) and (3):

$$DS_A = \frac{I_{acetyl} x7}{I_{AGU} x3} \tag{1}$$

$$DS_B = \frac{I_{butyryl} x7}{I_{AGU} x3} \tag{2}$$

$$DS_P = \frac{I_{propionyl} x7}{I_{AGU} x3} \tag{3}$$

where DS_A, DS_B and DS_P stand for the degree of substitution for acetyl, butyryl and propionyl, respectively. I_{AGU} stands for the intensity of the anhydroglucose units and $I_{acetyl/propionyl/butyryl}$ for the intensities of the methyl group in the respective side chain. The number 7 in the equations refers to the number of protons on the backbone and the number 3 refers to the available sites for substitution per anhydroglucose unit (Hadi et al., 2020). For peak assessments, see SI Table S2 and Figs. S1 to S12.

2.5. Hansen solubility parameters

The Hansen solubility parameters (HSP) include three different types of molecular interactions: the nonpolar interactions dispersive forces, the polar interactions caused by the molecules permanent dipole and hydrogen bonding (Hansen, 2007). The squared total HSP, δ_{tot}^2, is defined as the ratio between the total cohesive energy (E_{tot}) and the molar volume (V_{molar}). It can be expressed as the sum of the squares of dispersion (δ_D), polar (δ_P) and hydrogen bonding interactions (δ_H) according to Eq. (4):

$$\delta_{tot}^2 = \frac{E_{tot}}{V_{molar}} = \frac{E_D + E_P + E_H}{V_{molar}} = \delta_D^2 + \delta_P^2 + \delta_H^2 \tag{4}$$

The individual solubility parameters for each material were calculated via the method suggested by Hoftyzer and van Krevelen (VKH) (van Krevelen & Nijenhuis, 2009). The calculations are based on the list of the components for dispersive (F_d) and polar (F_P) forces, along with the hydrogen bond energy (E_h) and Fedor's molar volumes (V_F) of the different groups (Table 1).

The VKH equations for the different solubility parameters are calculated as follows:

$$\delta_d = \frac{\sum n_i F_{di}}{V_{molar}} = \frac{\sum n_i F_{di}}{\sum n_i V_{Fi}} \tag{5}$$

$$\delta_p = \frac{\sqrt{\sum n_i F_{pi}^2}}{V_{molar}} = \frac{\sqrt{\sum n_i F_{pi}^2}}{\sum n_i V_{Fi}} \tag{6}$$

$$\delta_h = \sqrt{\frac{\sum n_i E_{hi}}{V_{molar}}} = \sqrt{\frac{\sum n_i E_{hi}}{\sum n_i V_{Fi}}} \tag{7}$$

where the contribution from each group is weighted against an average degree of substitution (n_i) of each group in a monomer unit, which is

Table 1

The dispersion components (F_d), polar components (F_p), hydrogen bond energy components (E_h) and Fedor's molar volumes (V_F) of different groups (van Krevelen, 1990).

Group	F_d [$J^{1/2}$ cm$^{3/2}$ mol^{-1}]	F_p^2 [J cm^3 mol^{-2}]	E_h [J mol^{-1}]	Molar volumes, V_F [cm^3 mol^{-1}]
-COO-	390	240,100	7000	18
-CH3	420	0	0	33.5
-CH2-	270	0	0	16.1
>CH-	80	0	0	−1
-OH	210	250,000	20,000	10
-O-	100	160,000	3000	3.8
Ring ≥5	190	0	0	16

determined by NMR. This method is used due to its direct relation to the chemical structure and thus can be calculated from any structure. The experimentally determined values for CA, CAP and CAB are for discrete values of HSP and studies show a strong correlation between the degree of substitution and HSP (Bochek & Apetropavlovsky, 1992; Ramanaiah et al., 2011; Ramanaiah et al., 2012).

The HSP can be represented in a 3-dimensional space, where the distance Ra between the coordinates of two materials provides information of how similar they are with respect to solubility (Elidrissi et al., 2012; Gårdebjer, Andersson, et al., 2016; Gårdebjer, Gebäck, et al., 2016; Hansen, 2007), and can be calculated as:

$$(Ra)^2 = 4(\delta_{d2} - \delta_{d1})^2 + (\delta_{p2} - \delta_{p1})^2 + (\delta_{h2} - \delta_{h1})^2 \tag{8}$$

where 1 and 2 refer to the cellulose derivative and water, respectively.

2.6. Water absorption and permeation

The amount of water absorbed by the cellulose derivatives was determined via the increase in mass of 500 μm films kept in water for 72 h. The amount of water absorbed was calculated according to:

$$Percent\ water\ absorption = \frac{m_w - m_d}{m_d} \times 100 \tag{9}$$

where m_w is the wet weight of a film after excess water on the surface has been removed, and m_d is the dry weight of the film once it has been dried overnight in a Memmert Model 600 oven at 60 °C.

The water diffusion was determined by using custom made diffusion cells with two 20 mL chambers containing 15 mL deionized water each and separated by the film of interest with 8 mm diameter diffusion area, and the set-up is described elsewhere (Maciejewski et al., 2018; Larsson et al., 2010; Hjärtstam & Hjertberg, 1999b; van den van den Mooter et al., 1994). 10 μL of radio-labeled water (Tritium T_2O, 1 mCi g^{-1}) was added to the donor side, followed by the collection of 0.5 mL at predefined times from the acceptor side, while simultaneously replacing the same amount of dissolution medium. The experiments were carried out at room temperature and on a shaker. A quantity of 3 mL Ultima Gold was added to each sample before the amount of T_2O was measured using a PerkinElmer Tri-Carb 2810 TR liquid scintillation analyser. Five replicates were made for each material. The mass transfer of water was calculated using the method proposed by van den Mooter et al. (van den Mooter et al., 1994) and commonly used by others to determine water transport (Gårdebjer et al., 2018). It is derived from a macroscopical diffusion (Fick's law):

$$J = Ac\frac{D}{RT}\frac{\delta\mu}{\delta z} \tag{10}$$

where the mass transfer rate, J (mol s^{-1}), depends on the cross-section of the film, A (m^2), concentration, c (mol m^{-3}), diffusion coefficient, D (m^2 s^{-1}), universal gas constant, R (J K^{-1} mol^{-1}), absolute temperature, T (K), chemical potential, μ (J mol^{-1}) and distance through the film, z (m). From this expression, several assumptions are made: (i) the system is ideal and assumes that chemical potential depends on concentration, (ii) the concentration profile within the film is not time-dependent, (iii) stagnant layers at the film's surfaces have a negligent impact on permeation and, finally, (iv) there are equal volumes of media on both sides of the film. These assumptions result in the following equation:

$$\frac{2PA}{hV}t = -ln\left(\frac{C_{d,0} - 2C_a(t)}{C_{d,0}}\right) \tag{11}$$

where P is the permeability (m^2 s^{-1}), h (m) is the thickness of the film, V (m^3) is the volume of the donor and acceptor chamber, t (s) is the time, $C_{d,0}$ (mol m^{-3}) is the concentration on the donor side at time 0 and $C_a(t)$ (mol m^{-3}) is the concentration on the acceptor side at time t. The expression on the right-hand side of the Eq. (11) is plotted against time,

and the slope is used to calculate the permeability.

2.7. TGA and DSC

The degradation temperature was determined by subjecting 5–10 mg samples to thermogravimetric analysis (TGA) using a TGA/DSC 3+ Star System (Mettler Toledo, Switzerland). These samples were heated from 30 to 500 °C with a nitrogen flow of 60 mL min⁻¹ and at a heating rate of 10 °C min⁻¹. The degradation temperature (T_d) was measured using STARe Evaluation Software (Mettler Toledo), which takes the point of intersection of the tangent to the TGA curve at the point of maximum gradient and the starting-mass baseline.

Differential scanning calorimetry (DSC) was used to investigate the T_g and the melt temperature (T_m). Samples (approx. 4 mg) were analysed with a DSC 2 STARe system instrument (Mettler Toledo, Switzerland) using a nitrogen flow of 60 mL min⁻¹. The heating rate was 10 °C min⁻¹, with the material being heated up from 25 °C to 250 °C followed by a cooling step with a cooling rate of 10 °C min⁻¹. T_g was calculated using STARe software midpoint tool, and T_m at the melting peak on the first heating cycle. The software was also used to obtain the enthalpy of fusion by integrating over the melting peak at the first heating cycle, if it could be found. This can then be used to calculate the crystallinity according to the following equation:

$$\%Cryst = \frac{\Delta H_f}{\Delta H_f^o} \times 100 \qquad (12)$$

where ΔH_f is the enthalpy of fusion in J g⁻¹ (the area of the melting peak) and ΔH_f^o (J g⁻¹) is the enthalpy of fusion of a perfect crystal of cellulose acetate, which was proposed by Cerqueira et al. (Cerqueira et al., 2006) to be 58.8 J g⁻¹. However, no enthalpy of fusion for either a perfect crystal of cellulose acetate propionate/butyrate or ethyl cellulose was found in the literature, thereby making the comparison mute.

2.8. WAXS

The nanostructure of the different materials was investigated by applying wide-angle x-ray scattering (WAXS) using a Mat: Nordic X-Ray scattering instrument (SAXSLAB) equipped with a high brilliance Rigaku 003 X-Ray micro-focus, Cu-K_α radiation source ($\lambda = 1.5406$ Å) and a Pilatus 300 K detector. The unconditioned films were taped onto a sample holder to retain them in a fixed position, while powder and wet films were sandwiched between two Kapton windows to allow for measurements to be made in vacuum. The measurements were performed at a distance of 134 mm between sample and detector, with an exposure time of 300 s. The 2D scattering patterns collected were integrated radially to generate the scattering curve, and the Kapton signal was subtracted from each curve.

3. Results and discussion

3.1. Chemical structure

FTIR measurements (Fig. 1) confirm the structure of the cellulose acetates with the OH stretch at 3479 cm⁻¹, C-H stretching vibrations of the side chains at 2969–2879 cm⁻¹, CH₃ stretching at 2975–2880 cm⁻¹, stretching of the carbonyl C=O of the acyl at 1753 cm⁻¹, water hydration peak at 1632 cm⁻¹ and C-H bending in the -O(C=O)-CH₃ at 1384 cm⁻¹. The signal at 1236 cm⁻¹ decreases from CA to CABIII, which indicates a relation to the acetyl group and has in the literature been related to the C-O-C asymmetric stretching of the acetyl group (Cao et al., 2007; Hu et al., 2015; Lindblad et al., 2008). The signal at 1170 cm⁻¹ increases with increased contents of propionyl and butyryl, which correlates within the literature to the assigned asymmetric stretching of C-O-C where one of the carbon atoms belongs to the butyryl group. The signal at 1048 cm⁻¹ has been assigned to the C₁-O-C₄ stretch, which agrees with similar intensity for all derivatives as they all have glycosidic links. Fig. 1 also shows that the ethyl group in ethyl cellulose share most peaks with the cellulose acetate derivatives, except for the signals of the ester and acetyl groups.

Several of the IR signals change with an increase in chain length of the substituents, i.e. going from acetyl to propionyl or butyryl, respectively, the intensity of the C-Hₙ signals at 2969–2879 cm⁻¹ increases
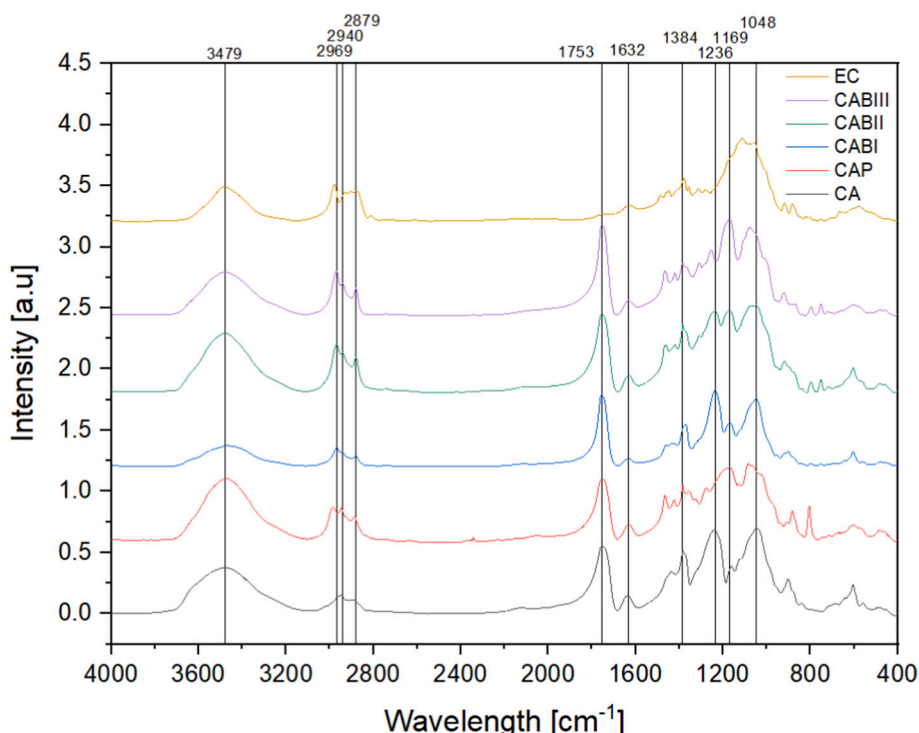

Fig. 1. FT-IR spectra of the different esters: CA, CAP, CABI, CABII, CABIII and EC, in ascending order.

compared to the OH signal, which is expected for the addition of further -CH$_2$ groups.

The DS of the various cellulose derivatives was extracted from NMR data, found in Figs. S1-S12 in the SI together with the calculation procedures. The NMR spectrum of cellulose acetate shows signals in two regions, where the protons of the anhydroglucose unit can be found between 3.2 and 5.5 ppm and the three methyl protons related to the acetyl group have signals at 2.05, 1.92 and 1.85 ppm. For CAP's acetyl methyl protons, a small shift to 1.97 and 1.89 was observed. Similar shifts of the acetate protons were seen for the CABs, with signals at 2.11–2.04, 1.99–1.97 and 1.92–1.89 ppm. The methylene groups of CAP give proton signals at 2.37 and 3.24 and those of CAB give 2.33, 2.2, 1.66 and 1.55 ppm. The methyl groups of CAP and CAB give proton signals at 1.17, 1.05 and 0.97, 0.89 ppm, respectively. This concurs with previous studies (Hikichi et al., 1995; Huang et al., 2011). EC has similar signals from the anhydroglucose unit and a methyl proton signal at 1.14 ppm.

The DS of the various side groups (Table 2) was determined and the total substitution, DS$_{tot}$, is defined as the sum of the DS of acetyl and propionyl/butyryl. The degree of hydroxyl group (DOH) was calculated as three minus DS$_{tot}$. The degree of substitution of the different esters confirms the observations seen in the FTIR data, where CABI to CABIII have an increasing number of butyryl substituents. The total degree of substitution is similar for all the derivatives, i.e. the variation is in the amount of the different substituents. Interestingly, the manufacturers provided ranges of DS, and these and the experimental obtained DS are very close to each other (see Table S1 in SI). The DSs were used to calculate the HSP of each material, and the solubility radius between water and the corresponding material.

3.2. Solid state characterization of films and processing

The degradation temperature (T$_d$), glass transition temperature (T$_g$) and melt temperature (T$_m$) are reported in Table 3. The T$_d$ was determined to establish that the processing temperatures to be well below the degradation temperature, see Fig. S13 for TGA curves and Figs. S14 to S15 for DSC heating curves in SI.

The T$_g$ of hot-melt pressed films decreases from a CA of 193 °C down to 109 °C for CABIII, indicating a clear impact of the DS$_B$. The DS$_P$ of CAP is like the DS$_B$ of CABIII, but the T$_g$ of CAP is closer to CABII, which implies that adding a CH$_2$ group to the side chain decreases the T$_g$ further. A decrease in T$_g$ is observed when the number of carbon atoms increases on the side chain in the order CA-CAP-CAB, meaning that T$_g$ decreases with increased side chain length and DS. This is in agreement with Teramoto, who observed a decrease in T$_g$ with an increase in the number of carbon atoms on the side chains for up to eight carbons (Teramoto, 2015). This trend could be because of an increased length of the side chain and DS, decreasing the possibilities for interactions between groups that can form hydrogen bonds in the cellulose derivatives, which will be further discussed below.

Table 3 shows that only CA and CABI films have a melting peak: CA at 230 °C and CABI 238 °C. The absence of melting peaks for the other films can be due to larger driving force to crystallize for CA and CABI

Table 3

Thermal properties of each film material, with corresponding data for powder in parentheses. Water absorption and water permeability of each material are also shown. TGA and DSC curves can be found in Figs. S13 to S15 in the SI.

Material	T$_d$ [°C]	T$_g$ [°C]	T$_m$ [°C]	ΔH_f [J g^{-1}]	Water abs [wt%]	Water permeation [10^{-12} m^2 s^{-1}]
CA	355	193 (191)	230 (233)	1.00 (7.74)	12.0 ± 2.0	5.0 ± 0.6
CAP	356	143 (140)	– (201)	– (4.14)	3.8 ± 0.2	1.2 ± 0.2
CABI	365	154 (155)	238 (241)	6 (10.64)	4.4 ± 0.2	1.9 ± 0.5
CABII	356	136 (137)	– (168)	– (11.17)	3.3 ± 0.1	0.8 ± 0.1
CABIII	353	109 (100)	– (143)	– (12.30)	1.8 ± 0.5	1.5 ± 0.2
EC	338	126 (121)	177 (174)	4.35 (6.40)	4.9 ± 0.2	2.1 ± 0.8

films, since their T$_m$ are larger than for the other polymers. The observed T$_m$ for CA is in the lower range compared to the literature (230–260 °C) whereas for CABI is in the upper range (130–240 °C) (Schuetzenberger, Dreyfus, & Dreyfus, 2016; Wypych, 2016). These deviations in T$_m$ between the values for CA and CABI in this study and the literature can be caused by different molecular weights and DSs, which can influence T$_m$. No melt peaks were observed for the other acetate films, whereas the starting powder material (in parenthesis) all show melt signals. The disappearance of a melting peak might be due to the film-forming process like cooling rate and/or the materials' high melt viscosity, which may affect the thermal properties of the resulting material significantly (Boy & Schulken, 1967). The area under the melting peaks represents the melting enthalpy. A decrease and disappearance of the melting peaks are related to a decrease in crystallinity, defined as the ration between the melting enthalpy and the enthalpy of fusion of a perfect crystal. For a CA crystal is this value 58.8 J g^{-1}, giving a crystallinity of 1.7% for CA film: this is lower than that is found in the literature, where Schuetzenberger et al. reported 12% (Schuetzenberger et al., 2016). In summary, the film-forming process has an enormous impact on thermal properties and for the hot-melt pressing used here, the crystallinity of the materials seems to decrease.

The effect of the hot-melt pressing process can also be observed with WAXS. In Fig. 2, black curves represent the powder used as received and red curves the hot-melt pressed films (for WAXS data plotted against 2θ, see SI Fig. S16) The crystallinity can be calculated from WAXS data for CA, according to An et al. (2019), but we have chosen not to include this approach in this study due to the difficulties verifying the used WAXS peaks for the different cellulose derivatives. However, one could observe significantly sharper peaks in the WAXS pattern for CAP and CABIII powder compared to the films: this can be explained by that the powders have been manufactured in such a way that they have achieved a more ordered structure and that, upon hot-melt pressing, the structure is becomes amorphous to a larger extent. CA and CABI show less significant change between powder and film, which might be due to their larger

Table 2

Degree of substitution calculated from NMR and calculations of the HSP (J cm^{-3})$^{1/2}$ using Table 1 and Eqs. (5) to (7). The HSP values of water are taken from Hansen (2007). Ra is the HSP distance between water and the different polymers.

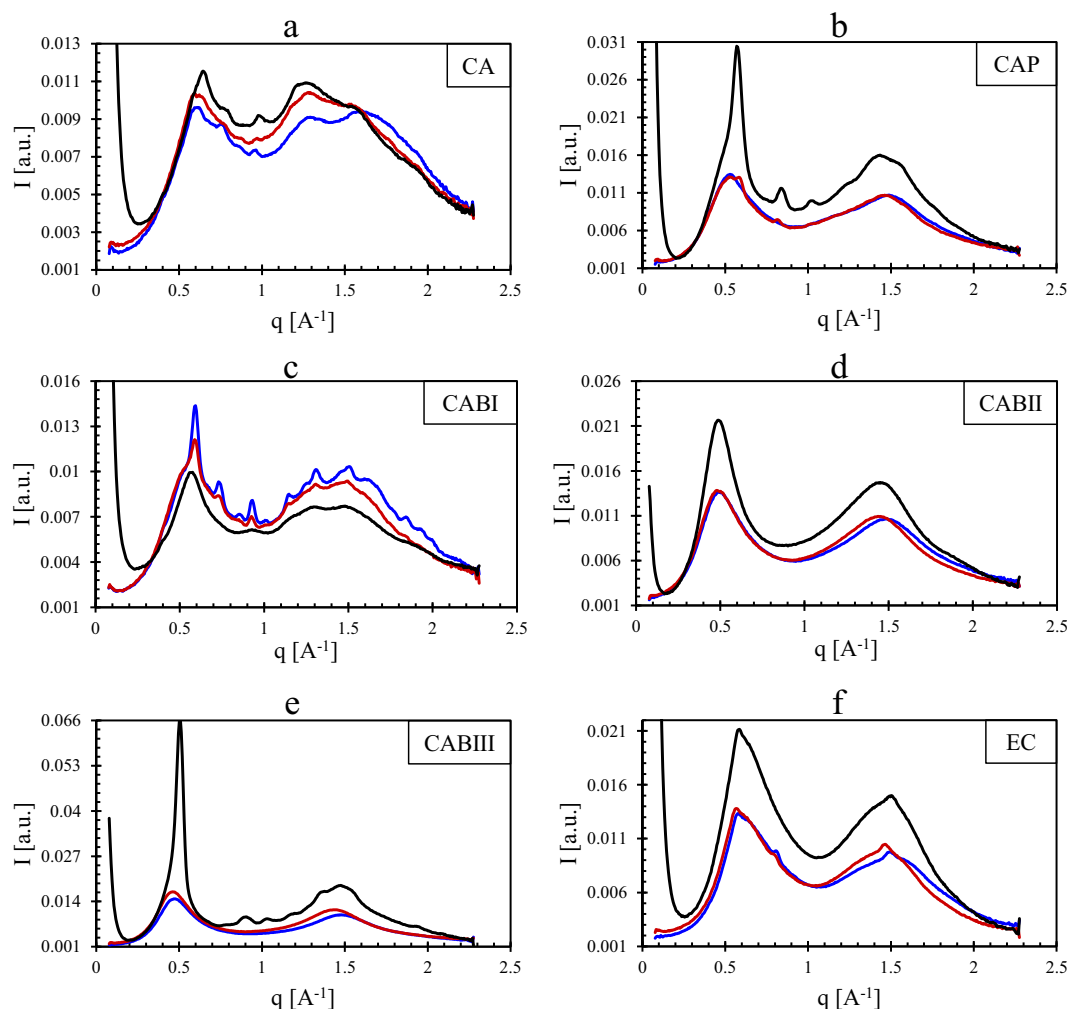| Material	DS$_{tot}$	DS$_A$	DS$_P$/DS$_B$	DOH	δ_d (J cm^{-3})$^{1/2}$	δ_p (J cm^{-3})$^{1/2}$	δ_H (J cm^{-3})$^{1/2}$	δ_{tot} (J cm^{-3})$^{1/2}$	Ra (J cm^{-3})$^{1/2}$
CA	2.41	2.41	–	0.59	19.0	6.2	14.5	24.7	30.3
CAP	2.85	0.21	2.64	0.15	18.2	4.5	11.3	21.9	33.5
CABI	2.85	2.14	0.71	0.15	18.4	5.0	11.9	22.4	32.9
CABII	2.80	1.12	1.68	0.20	18.2	4.3	11.2	21.8	33.6
CABIII	2.71	0.14	2.57	0.29	18.1	3.9	10.9	21.5	34.1
EC	2.56	–	–	0.45	18.1	5.2	11.3	22.0	33.2
Water	–	–	–	–	15.5	16	42.3	47.8	–

Fig. 2. WAXS curves for CA, CAP, CABI, CABII, CABIII and EC as powder (black), unconditioned films (red) and wet conditioned films (blue). For the 2θ curves, the reader is referred to SI, Fig. S16.

inter- and intramolecular interactions, shown as their larger T_m and T_g values relative to the other polymers and thus give rise to similar driving forces for the formation of the powders and films. To exclude differences in the manufacturing process of the powders, WAXS was also performed on precipitated materials, see SI Fig. S17. The WAXS for the precipitated and original powders were overall similar, with a small tendency that the precipitated samples appeared more crystalline than the original samples, probably because the precipitated samples being purified and crystallized easier. The difference between the precipitated and original powder was largest for CABI, and this polymer also shows small, sharp peaks arise in the melt pressed film and thereby increased crystallinity for both melt pressing and precipitation, indicating that the original powder being processed, so a less ordered structure was achieved. Although EC has an entirely different side chain to the esters, it shows a similar structure with two main peaks; it has a high intensity at 0.55 ± 0.1 Å^{-1}, like CAP and CAB, which could indicate that this peak is related to the carbohydrate chain. Similarly, for another system, Gu et al. assigned the signal at 0.5 Å^{-1} to correlate to the distance between adjacent main chains (Gu et al., 2012).

3.3. Cellulose derivative films and water

3.3.1. Structural change from water studied by WAXS

The WAXS graphs (Fig. 2) clearly show that when the hot-melt pressed films are submerged in water their structure is affected: the

red curves represent films conditioned at room temperature and the blue curves those submerged in water for one day. The largest difference was observed for CA, where the intensities of water-exposed films show a decrease at $q = 1.3$ Å^{-1} and an increase at higher q (1.6–2 Å^{-1}) caused by water absorption. Similar behaviour has been observed in regenerated cellulose when the water content was increased (Li et al., 2020). A slight shift of the peak at 1.45–1.5 Å^{-1} can be observed for EC, CABI, CABII, CABIII and CAP, being most prominent for EC and CABI. The shift to higher q can be interpreted as a decrease in the plane distance in the structure. This could be related to a water-induced plasticizing of the polymer, which could enable closer packing of the chains or a contribution of water itself. CA, EC and CABI absorb more water than the other polymers: this concurs with their findings of a larger water-induced change in structure. In addition to the shift from water, it appears that the water induces more prominent peaks for CA and CABI, which can be correlated to an increase in structural order. Thus, absorbed water softens the structure to a degree where local packing patterns increase and slightly increase the crystallinity. CAP, CABII and CABIII appear less affected, which agrees with their lower overall water absorption, which probably can be related to their increased hydrophobicity.

3.3.2. Influence of hydroxyl groups

The ability of water to dissolve in the different materials, here characterized as the materials' ability to absorb water, is presented in Table 3. It was highest for the CA film (12 ± 2 wt%), in alignment with

the 10–14% observation found in the literature (Zhang et al., 2012), followed by EC, CABI, CAP, CABII and CABIII in declining order. Fig. 3a and b shows a non-linear behaviour in DOH for both the T_g and water absorption. The initial decrease in DOH between 0.15 and 0.29 (where DOH = 0.29 corresponds to CABIII), gave decreased glass transition temperatures and water absorption, after which both properties increased instead. The water permeability was determined for the films, and it is known that crystallinity is an essential parameter for determining the diffusion rate (Gårdebjer et al., Trifol et al., 2020). However, for these hot-melt pressed films, the degree of crystallinity is low (≪10%), and therefore, no further discussion of the correlation of crystallinity to permeability will be performed. Interestingly, water permeation follows a similar trend as the T_g and water absorption relative DOH, but with CABII as the turning point. However, the major difference is that CABIII does not have the lowest permeation, despite having the lowest absorption of water. This can be due to the existence of microcracks that may be formed during the cooling step then the films are manufactured. The brittleness of CABIII's films and their propensity to break further supports the existence of microcracks, and it can also be emphasized that shaping CABII's films large enough for use in permeability measurements was challenging.

In the literature, it has been suggested that an increase in the amount of hydroxyl groups correlates to an increase in both the T_g and water absorption (Hjärtstam & Hjertberg, 1999a; Ong et al., 2013). Furthermore, Ong et al. have shown that solvent-cast CAP and CAB films increase water absorption with increasing DOH, for DOH values between 0.8 and 1.29. The reason why the present study does not show the same linear relation as Ong et al. may be explained by the difference in the method employed to prepare the film, or the different and smaller variations in the DOH, which was beneficial in our case for studying the effects of the molar structures of the substituents. The non-linear relationships observed between DOH and the T_g, water absorption and water permeation indicate that factors other than the number of OH groups seem to influence these properties. The effects of the molecular structures were investigated further by correlating the polymer properties to the HSP.

3.4. Hansen solubility parameters and material properties

The HSP divide the intermolecular interactions into dispersion (δ_D), polar (δ_P) and hydrogen bonding interactions (δ_H) (Hansen, 2007). The molar volumes are essential when calculating HSP, therefore the calculated V_{molar} were compared with experimentally determined ones. A linear relationship was found even though the total values deviated (see SI for the description of the experimental method, Fig. S18 and Table S3). This deviation may be due to either the experimental method or the calculation method, or indeed both. The linear relation nevertheless supports the trend of how the molar volumes vary for the studied cellulose derivatives. This section compares the HSP to the thermal properties and water interactions.

3.4.1. Glass transition temperature related to HSP

The different HSP are translated into cohesive energy per unit for each type of interaction (dispersive, polar and hydrogen bonding forces) by $E_i = \delta_i^2 V_{molar}$ and plotted against V_{molar}, Fig. 4. As V_{molar} increases, the energy for the dispersive force increases while the polar energy decreases slightly; the hydrogen bonding energy is basically constant. This is explained by that the dispersive forces increase as the methylene groups are added to the side chain, whereas only small changes in polar and hydrogen bonding groups occur. It is interesting to note that the dispersion energy E_d contributes most to the total cohesive energy density (>59%), followed by the hydrogen bonding energy (between 25 and 35%) and the very small fraction from the polar interaction (between 3 and 6%).

One hypothesis is that the T_g increases as the total cohesive energy per unit increases, thereby increasing the V_{molar} (Figs. 4 and 5). However, the opposite was in fact found: T_g decreases as V_{molar} increases. Comparing the T_g to the calculated V_{molar} (Fig. 5) shows a solid correlation for the esters, indicating that the V_{molar} impacts the T_g strongly. Fig. 6 was drawn to investigate whether the T_g could be related to the total cohesive energy density and/or any of the cohesive energy densities of the various types of interactions. As can be seen, T_g increases with increasing cohesive energy density for all three types of interaction in the HSP, and thus with the total cohesive energy density, with some deviations for EC. No single type of interaction appears to control the T_g. This shows that T_g decreases with both an increase in the V_{molar} and an increase in the dispersive forces. The latter originates from the increase in the van der Waal interactions when the length of the side chain increases. The reason for the reduced T_g is suggested to be due to the increased side chain length screens, both short distance hydrogen bonds as well as polar interactions within and between the polymer chains. Thus, as the dispersive forces and V_{molar} increase when methylene groups are added, the distance between the polymer backbones also increases, which in turn leads to a lesser likelihood of forming hydrogen bonds. Interestingly, the addition of just a few methylene groups decreases the T_g drastically between CA and CABI, which indicates a critical average side chain length after which the effect of hydrogen bonding decreases.

The different HSP parameters and the total HSP were compared to the T_g in Fig. 6. The T_g appears to increase overall with each of the HSP, with some deviations for EC. To explain this observation, the meaning of HSP must be reminded. The δ_h and δ_p decrease due to an increase in the V_{molar} as the side chain grows, Eqs. (5)–(7) and Table 2, while there is no addition of any polar and hydrogen bonding groups and thus no significant changes in these forces. In the case of δ_d, the dispersive force increases when methylene groups are added to the side chain, but at the same time, the V_{molar} increases and even more than the addition of dispersive forces, resulting in a net reduction of δ_d, Table 2. The increase
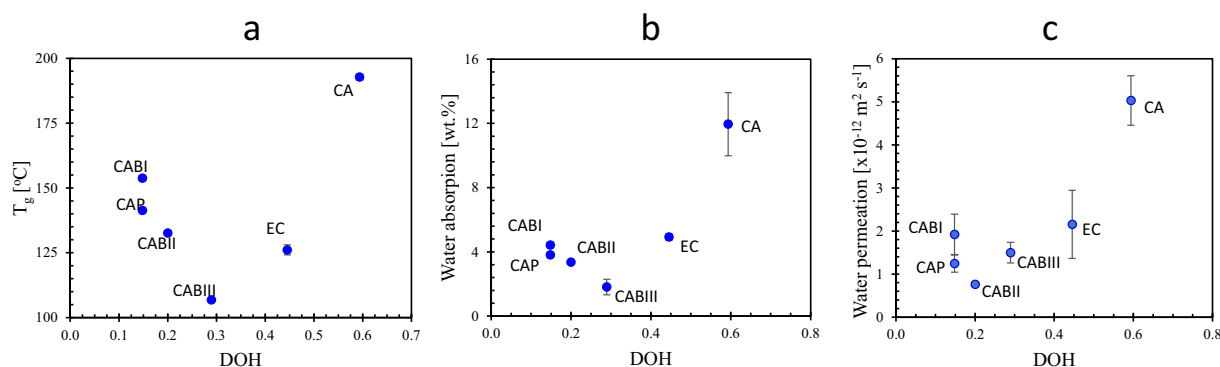

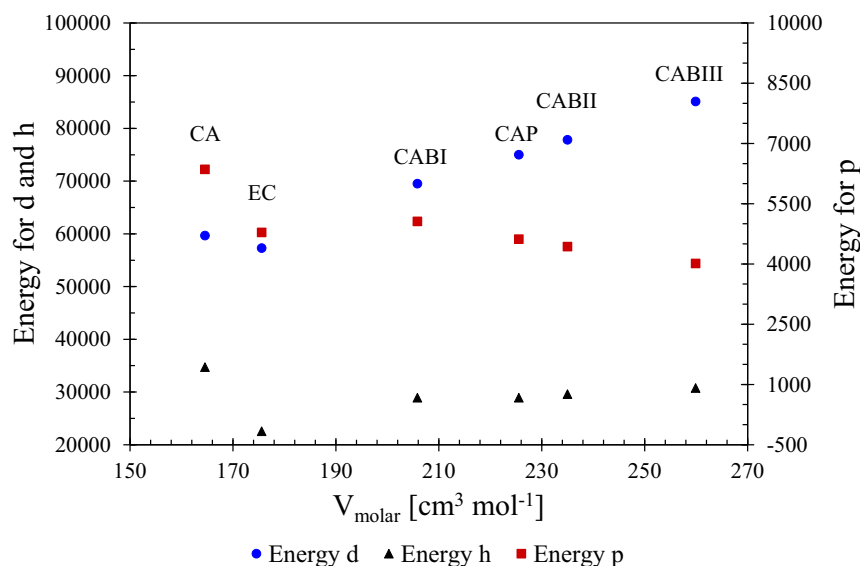**Fig. 3.** The relationship of DOH to a) T_g, b) water absorption and c) water permeation.

Fig. 4. The energy of dispersion and polar and hydrogen bonding vs. V_{molar}. Note, the polar energy axis is on the right-hand side.
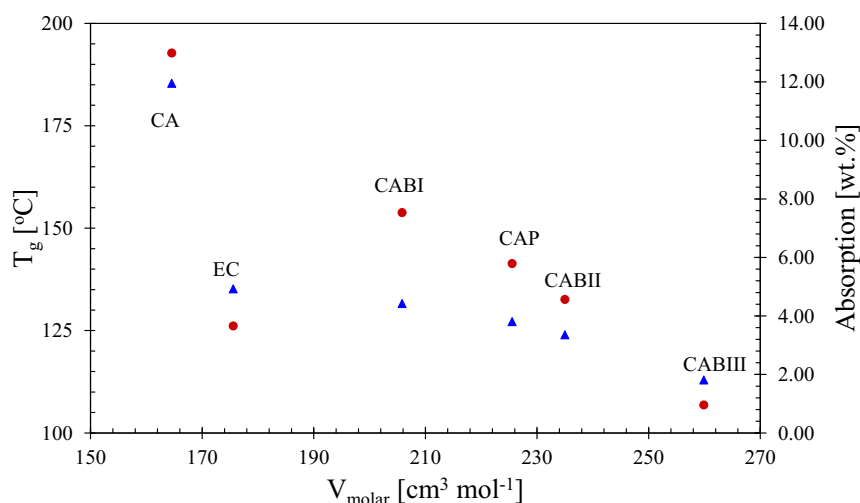

Fig. 5. T_g (circles) and water absorption (triangles) related to the V_{molar}.

of dispersive force could be assumed to increase the T_g, as the side chain length increases. In contrast, two factors should be noted in Fig. 6: first, a steady increase of T_g for all δ_is are observed, independent of which δ_i that is plotted, indicating that δ_d, has no exceptional position relative to other δ_is even if this parameter accounts for an increase in the dispersion energy, and, secondly, the T_g de facto decreases as the side chains become longer and the dispersive energy increases. However, Fig. 5 shows that as the lengths of the side chains increases, the V_{molar} increases and the T_g decreases, and therefore, V_{molar} is the more dominating factor than the addition of dispersion forces. The strong correlation for the esters in Fig. 5 also indicates that an increased V_{molar} causes an increased distance between the hydrogen bonding sites, as well as a lowering the total energy density (see δ_{tot}^2 in Table 2), which likely increases the chain mobility and thus decreases the T_g.

3.4.2. Water interactions related to HSP

The previous statement regarding the crucial distance between hydrogen bonding groups is even more pertinent for water interactions than for factors controlling the T_g. The water absorption was compared to the V_{molar}, Fig. 5, which shows, similar to T_g, that water absorption decreases with increasing V_{molar}. This can be explained by how water

interacts via dipole-dipole interactions and hydrogen bond. These interactions are affected by the separation of water and the groups forming hydrogen bonds, such as ester groups (-COO-), hydroxyl groups (-OH) and ether groups (-O—). The decrease in water absorption with V_{molar} and the addition of methylene groups, which enhances the volume more than the dispersion energy, explain why both water absorption and permeation increase with all the HSP in Fig. 7.

Fig. S19 in the SI shows the water absorption plotted against the differences in solubility parameters ($\Delta\delta_i$) between the cellulose derivatives and water. There are two parts in this: (i) when $\Delta\delta_p$ and $\Delta\delta_h$ for the materials increases, i.e. deviate more from the solubility parameters of water and becomes less similar to water, the level of water absorption decreases, which can be expected, and (ii), the opposite is observed for the dispersive parameter $\Delta\delta_d$. The behaviour for $\Delta\delta_d$ can be explained by looking at CA. It has the largest value for $\Delta\delta_d$ and the largest water absorption of the investigated cellulose derivatives due to the shortest side chain causing the least screening of the hydrogen bonding between the water and the hydrogen bonding domains in the polymer chains. As previously discussed, this can be explained by that the dispersive forces for cellulose derivatives increase the V_{molar} more than dispersive interactions, see Eq. (5), resulting in a decrease in δ_d, and thus an increase
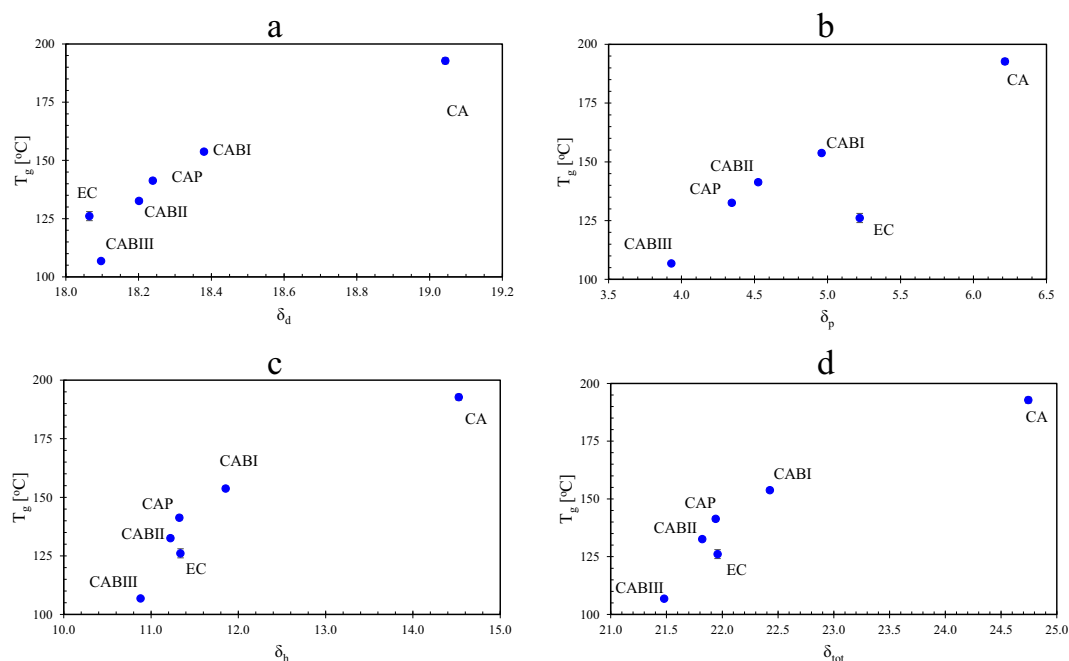
Fig. 6. T_g for the cellulose derivatives and how it relates to a) δ_d, b) δ_p, c) δ_H and d) δ_{tot}.

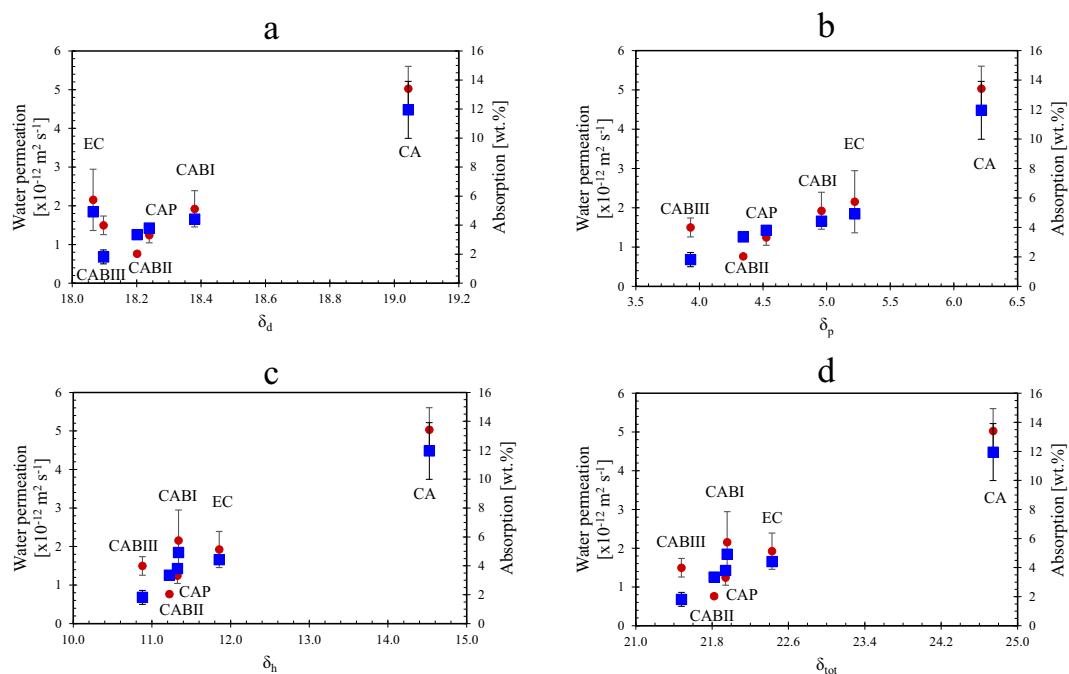**Fig. 7.** Water absorption (blue squares) and water permeation (red circles) of the different cellulose derivatives related to a) δ_d, b) δ_p, c) δ_H and d) δ_{tot}.

in $\Delta\delta_d$, and therefore is the water absorption increased when $\Delta\delta_d$ increases.

Fig. 4 illustrates how the hydrogen binding energy is basically constant for the different cellulose derivatives. As water molecules interact strongly via dipole-dipole interactions and hydrogen bonding, it may be expected that the introduction of water into cellulose esters relates to the two HSP that describe the interactions that originate from the permanent dipoles and their ability to form hydrogen bonds (δ_p and δ_h, respectively). This is not the case here, however, indicating that the hydrophobic side chains obstruct the water molecules from penetrating

the system and interacting with the hydrogen and polar groups located closer to the backbone of the polymer.

As far as the T_g is concerned, the interactions involved between two polymer chains have not been found to be dominated strongly by any individual HSP. It seems that, instead, the increase in V_{molar}, and thus separation of the hydrogen and polar interacting groups, control both the T_g and water absorption. The deviations seen in EC for T_g and water absorption in the HSP and V_{molar} plots suggest that making predictions of properties within the same type of cellulose derivatives is more reliable than making comparisons between different types of esters and

ethers: this indicates that other tools, like molecular dynamic simulations, could be employed advantageously.

4. Conclusions

This study shows that the total cohesive energy and the V_{molar} of cellulose esters increase upon the introduction of methylene groups, while an increase in the calculated cohesive energy, based on the Hansen model, is shown to decrease the T_g. The explanation suggested is that the increase in V_{molar} is greater than that of the cohesive energy, mainly added by the dispersive interactions, resulting in lower energy densities δ_{tot}^2. The introduction of methylene groups to the cellulose acetates creates a screening effect on the hydrogen bonding and polar interactions, which are short range interactions located close to the cellulose backbone. Thus, the change in the thermal properties can be related to the HSP and explained further by focusing on its building blocks, e.g. the V_{molar}.

The contributions made by the hydrogen bonding and polar energies to the cohesive energy are approximately constant for the cellulose derivatives in this study. This could have implied that the interactions with water should have been similar, but CA absorbs more than six times more water than CABIII. The addition of methylene groups decreases the hydrogen bonding and polar forces through a screening effect caused by the increase of the length of the side chains and thus increase in the V_{molar}, thereby explaining why water is hindered from penetrating into cellulose esters with long carbon chains, like CABIII.

The HSP provide insight into the interactions between different groups of cellulose esters and, to a certain degree, predict the effect of the length of the carbon chain in the substituent. Based on ethyl cellulose, however, this model appears to lack the ability to predict, accurately and precisely, the properties of materials from their chemical structure alone for all types of cellulose materials. This could be due to the lack of structural considerations being taken, such as the position of the groups relative to each other when calculating the HSP using the group addition method, implying that further development of such models is necessary.

This study shows that by choosing a number of methylene groups in the side chain of cellulose derivatives, the thermal properties and water interactions can be tailored. In summary, understanding how different substituents in cellulose derivatives affect thermal properties and how they interact and are affected by water can provide tools for tailoring derivatives with specific properties and thus the possibility of transferring from fossil-based to cellulose-based materials.

CRediT authorship contribution statement

Robin Nilsson: Conceptualization, Methodology, Validation, Formal analysis, Investigation, Resources, Data curation, Writing – original draft, Writing – review & editing, Visualization. **Martina Olsson:** Methodology, Validation, Formal analysis, Investigation, Writing – review & editing, Visualization. **Gunnar Westman:** Methodology, Formal analysis, Writing – review & editing, Visualization, Supervision. **Aleksandar Matic:** Methodology, Formal analysis, Writing – review & editing, Supervision, Funding acquisition. **Anette Larsson:** Conceptualization, Methodology, Formal analysis, Resources, Data curation, Writing – original draft, Writing – review & editing, Supervision, Project administration, Funding acquisition.

Declaration of competing interest

The authors declare that they have no known competing financial interests or personal relationships that could have influenced the work reported in this paper.

Appendix A. Supplementary data

Supplementary data to this article can be found online at https://doi.org/10.1016/j.carbpol.2022.119188.

References

Akim, E. L. (2005). Interaction of cellulose and other polysaccharides with water systems. *Chemistry of Polysaccharides, 63*(9), 221–293.

An, M., Zhang, Q., Ye, K., Lin, Y., Wang, D., Chen, W., … Li, L. (2019). Structural evolution of cellulose triacetate film during stretching deformation: An in-situ synchrotron radiation wide-angle x-ray scattering study. *Polymer, 182*(June). https://doi.org/10.1016/j.polymer.2019.121815

Andersson, H., Häbel, H., Olsson, A., Sandhagen, S., von Corswant, C., Hjärtstam, J., Persson, M., & Stading, Larsson (2016). The influence of the molecular weight of the water-soluble polymer on phase-separated films for controlled release. *International Journal of Pharmaceutics*. ISSN: 0378-5173, *511*(1), 223–235. https://doi.org/10.1016/j.ijpharm.2016.06.058

Andrade Alves, J. A., Lisboa dos Santos, M. D., Morais, C. C., Ramirez Ascheri, J. L., Signini, R., dos Santos, D. M., … Ramirez Ascheri, D. P. (2019). Sorghum straw: Pulping and bleaching process optimization and synthesis of cellulose acetate. *International Journal of Biological Macromolecules, 135*, 877–886. https://doi.org/10.1016/j.ijbiomac.2019.05.014

Asai, T., Taniguchi, H., Kinoshita, E., & Nakamura, K. (2001). Thermal and mechanical properties of cellulose acetates with various degrees of acetylation in dry and wet states. *Recent Advances in Environmentally Compatible Polymers, 275–80*. https://doi.org/10.1533/9781845693749.5.275

Ashley, R. J. (1985). *Permeability and Plastics Packaging. in Polymer Permeability*. In J. Comyn (Ed.) (pp. 269–308). Springer Netherlands. https://doi.org/10.1007/978-94-009-4858-7_7.

Bochek, A. M., & Petropavlovsky, G. A. (1993). Cellulose solubility parameters. *Cellulose Chemistry and Technology, 27*, 587–596.

Boy, R. E., Schulken, R. M., & Tamblyn, J. W. (1967). Crystallinity in secondary esters. *Journal of Applied Polymer Science, 11*, 2453–2465.

Cao, Y., Jin, W., Meng, T., Zhang, J., He, J., Li, H., & Zhang, Y. (2007). Acetone-soluble cellulose acetates prepared by one-step homogeneous acetylation of cornhusk cellulose in an ionic liquid 1-allyl-3-methylimidazolium chloride (AmimCl). *Carbohydrate Polymers, 69*(4), 665–672. https://doi.org/10.1016/j.carbpol.2007.02.001

Cerqueira, D. A., Filho, G. R., & Assunção, R. M. N. (2006). A new value for the heat of fusion of a perfect crystal of cellulose acetate. *Polymer Bulletin, 56*(4–5), 475–484. https://doi.org/10.1007/s00289-006-0511-9

Elidrissi, A., Barkany, S. E., Amhamdi, H., Maaroufi, A., & Hammouti, B. (2012). New approach to predict the solubility of polymers application: Cellulose acetate at various DS, prepared from Alfa 'Stipa -tenassicima' of Eastern Morocco. *Journal of Materials and Environmental Science, 3*(2), 270–285.

Filho, R., Guimes, D. S. M., da Silva Meireles, C., de Assunção, R. M. N., Cerqueira, D. A., Barud, H. S., … Messadeq, Y. (2008). Synthesis and characterization of cellulose acetate produced from recycled newspaper. *Carbohydrate Polymers, 73*(1), 74–82. https://doi.org/10.1016/j.carbpol.2007.11.010

Gabor, (. N). D., & Tita, O. (2012). Biopolymers used in food packaging: A review. *Acta Universitatis Cibiniensis Series E: Food Technology, XVI*(2), 3–19.

Gårdebjer, S., Andersson, M., Engström, J., Restorp, P., Persson, M., & Larsson, A. (2016). Using Hansen solubility parameters to predict the dispersion of nano-particles in polymeric films. *Polymer Chemistry, 7*(9), 1756–1764. https://doi.org/10.1039/c5py01935d

Gårdebjer, S., Gebäck, T., Andersson, T., Fratini, E., Baglioni, P., Bordes, R., Viridén, A., Nicholas, M., Lorén, N., & Larsson, A. (2016). The impact of interfaces in laminated packaging on transport of carboxylic acids. *Journal of Membrane Science, 518*, 305–312. https://doi.org/10.1016/j.memsci.2016.06.045

Gårdebjer, S., Larsson, M., Gebäck, T., Skepö, M., & Larsson, A. (2018). An overview of the transport of liquid molecules through structured polymer films, barriers and composites – Experiments correlated to structure-based simulations. *Advances in Colloid and Interface Science*. https://doi.org/10.1016/j.cis.2018.05.004

Gu, Y., Wang, C., & Russell, T. P. (2012). Multi-length-scale morphologies in PCPDTBT/PCBM bulk-heterojunction solar cells. *Advanced Energy Materials, 2*(6), 683–690. https://doi.org/10.1002/aenm.201100726

Hadi, N. A., Wiege, B., Stabenau, S., Marefati, A., & Rayner, M. (2020). Comparison of three methods to determine the degree of substitution of quinoa and rice starch acetates, propionates, and butyrates: Direct stoichiometry, FTIR, and 1H-NMR. *Foods, 9*(1). https://doi.org/10.3390/foods9010083

Hansen, C. M. (2007). *Hansen Solubility Parameters: A User's Handbook* (2nd ed.). CRC Press. https://doi.org/10.1201/9781420006834

Hikichi, K., Kakuta, Y., & Katoh, T. (1995). 1H NMR study on substituent distribution of cellulose diacetate. *Polymer Journal, 27*(7), 659–663. https://doi.org/10.1295/polymj.27.659

Hjärtstam, J., & Hjertberg, T. (1999a). Effect of hydroxyl group content in ethyl cellulose on permeability in free films and coated membranes. *Journal of Applied Polymer Science, 72*(4), 529–535. https://doi.org/10.1002/(sici)1097-4628(19990425)72:4<529::aid-app9>3.3.co;2-w

Hjärtstam, J., & Hjertberg, T. (1999b). Studies of the water permeability and mechanical properties of a film made of an ethyl cellulose-ethanol-water ternary mixture. *Journal of Applied Polymer Science, 74*(8), 2056–2062. https://doi.org/10.1002/(SICI)1097-4628(19991121)74:8<2056::AID-APP21>3.0.CO;2-Y

Hu, H., Li, H., Zhang, Y., Chen, Y., Huang, Z., Huang, A., Zhu, Y., Qin, X., & Lin, B. (2015). Green mechanical activation-assisted solid phase synthesis of cellulose esters using a co-reactant: Effect of chain length of fatty acids on reaction efficiency and structure properties of products. *RSC Advances, 5*(27), 20656–20662. https://doi.org/10.1039/c5ra02393a

Huang, K., Wang, B., Cao, Y., Li, H., Wang, J., Lin, W., Chaoshi, M., & Liao, D. (2011). Homogeneous preparation of cellulose acetate propionate (CAP) and cellulose acetate butyrate (CAB) from sugarcane bagasse cellulose in ionic liquid. *Journal of Agricultural and Food Chemistry, 59*(10), 5376–5381. https://doi.org/10.1021/jf104881f

Klemm, D., Heublein, B., Fink, H. P., & Bohn, A. (2005). Cellulose: Fascinating biopolymer and sustainable raw material. *Angewandte Chemie - International Edition, 44*(22), 3358–3393. https://doi.org/10.1002/anie.200460587

Kono, H., & Numata, J. (2020). Substituent distribution of propyl cellulose studied by nuclear magnetic resonance. *Carbohydrate Research, 495*(May), Article 108067. https://doi.org/10.1016/j.carres.2020.108067

Kreibch, U. T., & Batzer, H. (1979). Einfluß Der Segmentstruktur Und Der Vernetzung Auf Den Glasübergang Tg. Möglichkeiten Der Vorausberechnung von Tg Über Die Kohäsionsenergie Ecoh. *Die Angewandte Makromolekulare Chemie, 83*(1), 57–112. https://doi.org/10.1002/apmc.1979.050830105

Larsson, M., Hjärtstam, J., Berndtsson, J., Stading, M., & Larsson, A. (2010). Effect of ethanol on the water permeability of controlled release films composed of ethyl cellulose and hydroxypropyl cellulose. *European Journal of Pharmaceutics and Biopharmaceutics, 76*(3), 428–432. https://doi.org/10.1016/j.ejpb.2010.09.007

Lee, W. G., Kim, D. Y., & Kang, S. W. (2018). Porous cellulose acetate by specific solvents with water pressure treatment for applications to separator and membranes. *Macromolecular Research, 26*(7), 630–633. https://doi.org/10.1007/s13233-018-6091-3

Li, H., Kruteva, M., Mystek, K., Dulle, M., Ji, W., Pettersson, T., & Wågberg, L. (2020). Macro- and microstructural evolution during drying of regenerated cellulose beads. *ACS Nano, 14*(6), 6774–6784. https://doi.org/10.1021/acsnano.0c00171

Lindblad, M. S., Keyes, B. M., Gedvilas, L. M., Rials, T. G., & Kelley, S. S. (2008). FTIR imaging coupled with multivariate analysis for study of initial diffusion of different solvents in cellulose acetate butyrate films. *Cellulose, 15*(1), 23–33. https://doi.org/10.1007/s10570-007-9173-5

Lonsdale, H. K., Merten, U., & Riley, R. L. (1965). Transport properties of cellulose acetate osmotic membranes. *Journal of Applied Polymer Science, 9*(4), 1341–1362. https://doi.org/10.1002/app.1965.070090413

Maciejewski, B., Ström, A., Larsson, A., & Sznitowska, M. (2018). Soft gelatin films modified with cellulose acetate phthalate pseudolatex dispersion-structure and permeability. *Polymers, 10*(9). https://doi.org/10.3390/polym10090981

Ong, R. C., & Chung, T. S. (2012). Fabrication and positron annihilation spectroscopy (PAS) characterization of cellulose triacetate membranes for forward osmosis. *Journal of Membrane Science, 394–395*, 230–240. https://doi.org/10.1016/j.memsci.2011.12.046

Ong, R. C., Chung, T. S., Helmer, B. J., & De Wit, J. S. (2012). Novel cellulose esters for forward osmosis membranes. *Industrial and Engineering Chemistry Research, 51*(49), 16135–16145. https://doi.org/10.1021/ie302654h

Ong, R. C., Chung, T. S., Helmer, B. J., & De Wit, J. S. (2013). Characteristics of water and salt transport, free volume and their relationship with the functional groups of novel cellulose esters. *Polymer, 54*(17), 4560–4569. https://doi.org/10.1016/j.polymer.2013.06.043

Qiao, Z., Wang, Z., Zhang, C., Yuan, S., Zhu, Y., & Wang, J. (2012). PVAm–PIP/PS composite membrane with high performance for CO2/N2 separation. *AIChE Journal, 59*(4), 215–228. https://doi.org/10.1002/aic

Ramanaiah, S., Reddi Rani, P., & Reddy, K. S. (2012). Hansen solubility parameters for the solid surface of cellulose acetate propionate by inverse gas chromatography. *Journal of Macromolecular Science, Part B: Physics, 51*(11), 2191–2200. https://doi.org/10.1080/00222348.2012.669681

Ramanaiah, S., Reddi Rani, P., Sreekanth, T. V. M., & Reddy, K. S. (2011). Determination of Hansen solubility parameters for the solid surface of cellulose acetate butyrate by inverse gas chromatography. *Journal of Macromolecular Science, Part B, 50*(3), 551–562. https://doi.org/10.1080/00222341003784527

Reid, D. S., & Levine, H. (1991). Beyond water activity: Recent advances based on an alternative approach to the assessment of food quality and safety. *Critical Reviews in Food Science and Nutrition, 30*(2–3), 115–360. https://doi.org/10.1080/10408399109527543

Schuetzenberger, P., Dreyfus, C., & Dreyfus, H. (2016). CA cellulose acetate. In George Wypych (Ed.), *Handbook of Polymers* (2nd, pp. 33–38). ChemTec. https://doi.org/10.1016/B978-1-895198-92-8.50012-4.

Sun, X., Canhui, L., Zhang, W., Tian, D., & Zhang, X. (2013). Acetone-soluble cellulose acetate extracted from waste blended fabrics via ionic liquid catalyzed acetylation. *Carbohydrate Polymers, 98*(1), 405–411. https://doi.org/10.1016/j.carbpol.2013.05.089

Teramoto, Y. (2015). Functional thermoplastic materials from derivatives of cellulose and related structural polysaccharides. *Molecules, 20*(4), 5487–5527. https://doi.org/10.3390/molecules20045487

Trifol, J., Plackett, D., Szabo, P., Daugaard, A. E., & Baschetti, M. G. (2020). Effect of crystallinity on water vapor sorption, diffusion, and permeation of PLA-based nanocomposites. *ACS Omega, 5*(25), 15362–15369. https://doi.org/10.1021/acsomega.0c01468

van Krevelen, D. W., & Nijenhuis, K. T. (2009). Cohesive properties and solubility. *Properties of Polymers, i.* https://doi.org/10.1016/b978-0-08-054819-7.00007-8

van den Mooter, G., Samyn, C., & Kinget, R. (1994). Characterization of colon-specific azo polymers: A study of the swelling properties and the permeability of isolated polymer films. *International Journal of Pharmaceutics, 111*(2), 127–136. https://doi.org/10.1016/0378-5173(94)00102-2

van Krevelen, D. W. (1990). *Properties of polymers: Their correlation with chemical structure; their numerical estimation and prediction from additive group contributions*. Elsevier. 10.1016/B978-0-444-82877-4.50014-7.

Viriden, A., Larsson, A., Schagerloef, H., & Bengt, W. (2010). Model drug release from matrix tablets composed of HPMC with different substituent heterogeneity. *International Journal of Pharmaceutics, 401*(1–2), 60–67. https://doi.org/10.1016/j.ijpharm.2010.09.017

Wypych, G. (2016). CAB cellulose acetate butyrate. In *, 39–42. Handbook of polymers*. https://doi.org/10.1016/b978-1-895198-92-8.50013-6

Zhang, S., Zhang, R., Jean, Y. C., Paul, D. R., & Chung, T. S. (2012). Cellulose esters for forward osmosis: Characterization of water and salt transport properties and free volume. *Polymer, 53*(13), 2664–2672. https://doi.org/10.1016/j.polymer.2012.04.024